Published in final edited form as:
Chemosphere. 2020 December ; 260: 127566. doi:10.1016/j.chemosphere.2020.127566.

Novel ball-milled biochar-vermiculite nanocomposites effectively adsorb aqueous As(Ⅴ)

Fang Li[a,b], **Yongshan Wan**[c], **Jianjun Chen**[d], **Xin Hu**[e], **Daniel C.W. Tsang**[f], **Hailong Wang**[g], **Bin Gao**[b,*]

[a]College of economics and management, Shandong Agricultural University, Tai'an 271018, China

[b]Department of Agricultural and Biological Engineering, University of Florida, Gainesville, FL, USA

[c]Center for Environmental Measurement and Modeling, US EPA, Gulf Breeze, FL 32561, USA

[d]Mid-Florida Research & Education Center, University of Florida, Apopka, FL 32703, USA

[e]Center of Material Analysis, Nanjing University, Nanjing 210093, PR China

[f]Department of Civil and Environmental Engineering, The Hong Kong Polytechnic University, Hong Kong, China

[g]School of Environmental and Chemical Engineering, Foshan University, Foshan, Guangdong 528000, China

Abstract

Ball milling was used to fabricate a nanocomposite of 20% hickory-biochar (600°C) and 80% expanded vermiculite (20%-BC/VE). This novel adsorbent had much higher As(V) removal efficiency from aqueous solution than ball-milled biochar (bm-BC) and ball-milled expanded vermiculite (bm-VE). Characterization of these adsorbents showed that enhanced As(V) adsorption was ascribed to much larger surface area and pore volume (2–6 times), notable changes in crystallinity, activation of cations, and increased functional groups in the nanocomposite compared with its pristine counterparts. The As(V) adsorption process by the nanocomposite fitted well with the pseudo-second-order kinetics model and Langmuir isotherm model, with a maximum adsorption capacity of 20.1 mg g^{-1}. The 20%-BC/VE best performed at pH about 6. The adsorption efficiency was not sensitive to the competition of NO_3^-, Cl^-, SO_4^{2-}, as well as the coexistence of humic acid. However, the adsorption capacity for As(V) was significantly reduced by coexisting with PO_4^{3-}. The 20%-BC/VE composite can potentially serve as a superior low-cost adsorbent for As(V) removal in real world applications.

Capsule:

Nanocomposites fabricated from proper proportions of biochar and vermiculite through ball milling effectively remove arsenic from aqueous solutions

*Corresponding author, Fax: (352) 392-4092, bg55@ufl.edu.

Keywords

Ball milling; Vermiculite; Biochar-based nanocomposites; Arsenic adsorption; Wastewater treatment; Sustainable waste management

1. Introduction

Arsenic (As) is a ubiquitous “metalloid”, abundantly distributed in the continental crust of the earth at concentrations of about 1.5–2 mg/kg (National Research, 1977). High arsenic-bearing parent rock weathering and volcano eruption are the source of most naturally occurring arsenic. Anthropogenic activities such as smelting and mining activities, the use of pesticides and herbicides, and the paint and cosmetic industry have resulted in elevated levels of arsenic in soil, atmosphere, hydrosphere and biosphere (Singh et al., 2015). It is reported that anthropogenic emissions of arsenical compounds amount to 24,000 tons per year, three times higher than natural emissions (Benbrahim-Tallaa and Waalkes, 2008). Arsenic pollution has caused global human health concerns due to its high carcinogenicity and pathogenicity for respiratory and immune system, and even lethality. Dermal lesions, cardiovascular disease, liver disease, neuropathy, and cancer are originally recognized adverse effects caused by arsenic exposure (National Research, 1999, 2001). The contamination of drinking water and food are two major human exposure pathways to As. It is reported that most of the global rice-producing regions are contaminated with high As concentration (Suriyagoda et al., 2018), which is partly due to irrigation with high As water.

Inorganic arsenic is characterized with stronger mobility and toxicity than organic arsenic (Huang and Matzner, 2006). The toxicity of arsenite (As(III)) is considered to be about 60 times larger than arsenate (As(V)) (Sattar et al., 2019). Naturally, As(III) is unstable due to oxidation caused by environmental factors such as pH and redox potential. Sugawara and Kanamori (1964)) showed that As(V) accounts for 80% of total arsenic in ocean water. Oxidation strategies, including photochemical oxidation, photocatalytic oxidation, biological oxidation, are common methods used to transform As(III) to less toxic As(V) (Gude et al., 2018; Lu et al., 2019; Shumlas et al., 2016).

The removal of arsenic in solution by adsorption is currently the most studied and the most widely used method among different arsenic treatments (Singh et al., 2015). Iron oxides (Aredes et al., 2013), magnesium oxide (Liu et al., 2011b), and aluminum oxide (Li et al., 2016b), are promising adsorbents for As remediation, for their high treatment capacities. Expanded vermiculite (VE) is commercially used as plant breeding substrate and possesses excellent adsorptive and coagulative properties (Miner, 1934). VE is an inexpensive, natural phyllosilicate material, featuring a sandwiched structure with large internal surface area, high cation exchange capacity, and high negative charge on the silicate layers (Tuchowska et al., 2019). Hence, it has been widely studied for adsorption of cationic dyes and heavy metals (Basaleh et al., 2019; Malandrino et al., 2011). The abundance of metallic oxides such as aluminum, magnesium, and iron in vermiculite, enables its potential for arsenic remediation (A. Saleh et al., 2016; Manning and Goldberg, 1996).

Impregnating adsorbents on support materials can improve As adsorption performance and reduce costs (Tuchowska et al., 2019; Zhang et al., 2004). Biochar as a novel adsorbent derived from pyrolysis of waste carbonaceous biomass, has drawn substantial attention for its large specific surface area, abundant functional group, and porous structure (Hu et al., 2015). It is also reported that ball milling is a viable and cost-effective technique that utilizes mechanical energy to grind pristine materials into nanoscale particles to enhance its physicochemical and sorptive properties (Lyu et al., 2018). Our preliminary trials confirmed that ball-milled vermiculite-biochar nanocomposite possesses strong affinity to anionic dye Red (RR120) (Figure S1). However, there are no reports in the literature about ball-milled vermiculite-biochar composite as an adsorbent to treat arsenic-containing wastewater.

In this work, biochar-vermiculite nanocomposites of different ratios were fabricated via ball milling. The adsorption efficiency of these adsorbents was studied through batch experiments. The main objectives of this work are to: (1) characterize the physicochemical properties of ball-milled vermiculite, biochar, and their nanocomposites, (2) determine the optimal biochar and vermiculite weight ratio (BC/VE) for As(V) adsorption, (3) evaluate the As(V) adsorption kinetics and isotherm of the BC/VE nanocomposites, and (4) investigate the influences of pH, anionic competition, and dissolved humic acid, on As(V) adsorption onto vermiculite-biochar nanocomposites.

2. Materials and methods

2.1 Materials

The raw VE was obtained from Low's Garden Center as an ordinary horticultural substrate. The main components of the vermiculite are SiO_2, Al_2O_3, MgO, Fe_2O_3, K_2O, and CaO (A. Saleh et al., 2016; Gencel et al., 2014). The VE were rinsed twice with deionized (DI) water (18.2 MΩ) (Nanopure water, Barnstead) and dried at 80ºC in an oven until the sample weight remained constant. Commercial hickory wood chips were purchased from Cowboy Charcoal, LLC (Stockton, CA). The wood was chopped and sieved to about 2 mm long with a mechanic mill (Thomas-Wiley, model 4). Sodium arsenate dibasic heptahydrate ($Na_2HAsO_4{\cdot}7H_2O$), humic acid, hydrochloric acid (HCl), and sodium hydroxide (NaOH) are all analytical pure grade, and purchased from Fisher Scientific.

2.2 Preparation of adsorbents

The biochar (BC) was fabricated from the crushed hickory wood chips following the procedure of Zheng et al. (Zheng et al., 2019a). Briefly, the crushed hickory wood chips were heated at 105 °C for 0.5 h, and then pyrolyzed by a tube furnace (Olympic 1823HE) at 600 °C under reducing atmosphere (N_2) for 1 h. The obtained BC was rinsed with DI water, and heated in an oven at 80°C to remove moisture until reaching a constant weight.

The ball-milling method described by Lyu et al. was used to synthesize VE and BC composites (Lyu et al., 2018). About 1.8 g raw material was placed within agate jars (500 mL) with beads (diameter ¼6 mm, 180 g), and then placed in a planetary ball mill machine (PQ-N2, Across International, New Jersey, USA). The operation parameters of the ball mill machine were set at 300 rpm for 12h with rotation direction altered every 0.5 h. The

pristine BC, VE, and the BC/VE mixtures at weight ratios of 1:9, 1:4, 3:7, and 2:3 were ball milled under the same milling conditions. The ball-milled particles were denoted as bm-BC, bm-VE, 10%-BC/VE, 20%-BC/VE, 30%-BC/VE, and 40%-BC/VE, whereby the percentages are BC contents in the composite. All the samples were stored separately in sealed containers for future use.

2.3 Characterization of adsorbents

To detect the microscopic structure of BC, VE and their composites, a field emission scanning electron microscopy (SEM; HITACHI, S-4800) equipped with an energy-dispersive X-ray spectroscopy (EDS; Horiba, EMAX) was used. The X-ray diffraction (XRD) analysis was performed to identify the crystallographic structure using a goniometer D8 ADVANCE Theta/Theta X-ray power diffractometer (Bruker Corporation, Karlsruhe, Germany), in a scanning range of 10 to 80° (2Θ) with a step size of 0.02°. The specific surface area (SSA), pore size and volume of the composites were measured using a Micromeritics AsAP 2460 instrument, according to Nitrogen adsorption-desorption method, Brunauer-Emmett-Teller (BET) and Barrett–Joyner–Halenda (BJH) theories. X-ray photoelectron spectroscopy (XPS, ESCALAB 250) was used to investigate the composition and speciation of surface elements, at the mode of Al anode X-ray exciting source (Al Kα=30 eV, step size=0.05eV). Fourier transform infrared spectra (FTIR) of the samples were recorded using a Bruker Vector 22 FTIR spectrometer (OPUS 2.0 software) (Zhang et al., 2013b). AB-250 pH meter (Accumet, Fisher Scientific, USA) was used to measure the solution pH.

2.4 Arsenic adsorption experiments

Stock solution of As (V) at 1 g L^{-1} was prepared by dissolving 4.16 g $Na_2HAsO_4{\cdot}7H_2O$ into 1L DI water. This stock lotion was diluted with DI water to obtain various solution concentrations required in the following batch experiments.

The arsenic sorption capacity of the ball-milled BC/VE composites at varying mixing ratios along with the raw-BC, bm-BC, and raw-VE samples was examined by mixing 50 mg BC/VE with 50 mL arsenic solutions (20 mg L^{-1}) in 68 mL conical centrifuge vessels at room temperature (25± 0.5 °C). The mixture was shaken at 220 rpm on a mechanical shaker for 48 h. Then the mixtures were immediately filtered through 0.45 μm nylon membrane filters. The arsenic concentrations in solutions were determined using ICP-OES. The adsorption capacity of adsorbents was calculated based on the initial and final arsenic concentrations in aqueous solutions. The experiment was replicated twice with additional experiments conducted whenever the relative difference was larger than 5%.

The rest of the batch experiments were conducted on the BC/VE composite having the highest As(V) adsorption capacity in a similar fashion as the above. Adsorption kinetics experiments were sampled at specific time intervals (i.e., 0, 0.083, 0.167, 0.5, 1, 2, 5, 10, 12, 24, 36, 48, and 56 h). Isotherm experiments were examined with arsenic concentrations ranging from 1 mg L^{-1} to 200 mg L^{-1}. The effect of solution pH was determined by varying the initial solution pH from 4 to 8. The anionic competition was determined by adding the same number of moles of sulfate ions (SO_4^{2-}), nitrate ions (NO_3^-), chloride ions (Cl^-), and

phosphate ions (PO_4^{3-}) with As(V). The effect of humic acid was examined by adjusting the humic acid concentration to 1, 5, 8, 10 mg L^{-1}. The details of the fitting adsorption kinetics and isotherm models were listed in the supporting information (S1, S2).

3. Results and discussion

3.1 Effects of the BC/VE weight ratio on arsenic removal capacities

In order to optimize As(V) adsorption efficiency, the ball-milled BC/VE nanocomposite in different weight ratios was examined and compared with their pristine counterparts (Figure 1). The raw-BC, bm-BC, and raw-VE samples had no adsorption of arsenic, while ball milling enhanced the ability of raw-VE to adsorb As(V). The ball-milled BC/VE nanocomposites were much more effective in adsorbing As(V) than bm-BC and bm-VE, suggesting positive synergy with ball milling. A comparison among the BC/VE nanocomposites (BC weight ratio of 10%−40%) showed that the 20%-BC/VE possessed the highest adsorption capacity for As(V), 6.89 mg g^{-1}, which was 47.3%, 15.6%, and 79.7% higher than that of 10%-BC/VE, 30%-BC/VE, and 40%-BC/VE. Since 20% biochar was the optimal weight ratio, the 20%-BC/VE nanocomposite was explored further in subsequent characterization and batch sorption experiments.

3.2 Characterization of materials

Table 1 lists the BET parameters of raw-BC, bm-BC, raw-VE, bm-VE, and 20%-BC/VE. The specific surface area (SSA) and pore volume (PV) of 20%-BC/VE were in between those of bm-BC and bm-VE. The SSA and PV of bm-VE were 2.866 m^2 g^{-1} and 0.0188 cm^3 g^{-1}, respectively, similar to the results (SSA=9 m^2 g^{-1}, PV=0.0072 cm^3 g^{-1}) in previous research of other VE samples (Silva et al., 2018). Ball milling reduced the SSA and PV of VE, likely caused by the destruction of the 2:1 crystalline structures of magnesium aluminum silicate in VE (Liu et al., 2011a; Shen et al., 1996). The mechanical activation by ball milling might have resulted in the storage of excess enthalpy and enhanced the reactivity of the material, which are beneficial to the adsorption of As(V) (Aglietti and Lopez, 1992; Li and Hitch, 2016). The addition of a small amount of BC particles dramatically increased the SSA and PV of the BC/VE composites compared with bm-VE, likely due to the contribution of the porous BC particles (Jin and Dai, 2012). The pore size of 20%-BC/VE sample was between that of bm-BC and bm-VE. The pore size distribution information is exhibited by the method of dV/dlog(W) Pore Volume vs. Pore Width (Figure 2S). The addition of BC significantly increased the pore size distribution of the 20%-BC/VE particle in the range of less than 15 nm, and remarkably produced large pores with the size of 60 nm. This suggests that ball milling can extrude BC particles into the interlayer of VE (Li et al., 2016a).

SEM-EDS analysis was used to characterize the surface morphology and microstructure of the adsorbents. The images show that the bm-BC particles were approximately 0.5 um, i.e., 5 to 10 times smaller than the median diameters of bm-VE particles (Figure 2a and c). These ultrafine particles were attached on the surface of larger bm-VE particle in the 20%-BC/VE sample (Figure 2(e)). To further evaluate the distribution of BC in the hybrid adsorbent, SEM-EDS was employed to characterize the element content. Compared with the

EDS-spectra of bm-VE, 20%-BC/VE sample was rich in carbon and nitrogen, indicative of successful incorporation of BC into the hybrid particles (Figure 2(d and f)).

The XRD analysis was used to identify the mineral and metal components in bm-BC, bm-VE, and 20%-BC/VE samples. As shown in Figure 3 (a), only the XRD pattern of bm-VE sample shows the strong peaks at 27° and 7°. And SiO_2 (quartz and silicon oxide), $AlPO_4$ (Berlinite), $Al_2Si_2O_5(OH)_4{\cdot}2H_2O$ (Halloysite), and $KMg_3(Si_3Al)O_{10}(OH)_2$ (Phlogopite) were identified in raw-VE through standard curve comparison (Yao et al., 2016). Only broad diffraction peaks with low intensity were identified in bm-BC (Zheng et al., 2019b). However, there were no obvious diffraction peaks in the XRD pattern of 20%-BC/VE in spite of 80% VE in the nanocomposite, suggesting that ball milling with BC reduced VE's mineral crystallinity and thus might increase the surface mineral adsorption sites. This result suggests that the nanocomposite of two raw materials fabricated by ball milling caused notable changes to the crystallinity of VE.

The absorption peaks of FTIR spectrums within 400–3400 cm^{-1} were used to determine the particular functional groups in bm-BC, bm-VE, and 20%-BC/VE. As shown in Figure 3 (b), the stretching vibration bands at around 3431 cm^{-1} and the absorption peak at 1656 cm^{-1} of bm-VE can be ascribed to -OH and H-O-H of the structure water molecule (Basaleh et al., 2019). The C-H and C=C asymmetrical stretching vibrations appeared at 2359 and 2330 cm^{-1} (Alzaydien, 2016). The peak at 759 cm^{-1} was regarded with the bending vibration of Al-OH. The bands detected at 1057, 691, and sharp peak at 465 cm^{-1} were assigned to the stretching mode of Si-O, Si-O-Si, and Si-O-Mg groups (A. Saleh et al., 2016). The addition of biochar did not cause a noticeable change in the FTIR spectrum of 20%-BC/VE comparing with the bm-BC. Only two new strong peaks at 1588 and 1423 cm^{-1} appeared, which might correspond to the two peaks at 1580 and 1429 cm^{-1} of biochar. The 1588 cm^{-1} peak could be assigned to the stretching mode of aromatic N-H/C=C/C=O groups, while the 1429 cm^{-1} peak could be identified as C–N stretching group (Basaleh et al., 2019). In addition, the broaden bending vibration at about 3320 cm^{-1} might be assigned to the increasing of O-H/N-H groups bending deformation introduced by biochar (Ben Ticha et al., 2016). The overall result indicates that incorporating biochar into vermiculite by ball milling increased the amounts of functional groups in the adsorbent.

The characteristic binding energy of XPS spectra of the bm-BC, bm-VE, and 20%-BC/VE is shown in Figure 3 (c), confirming that the ball-milling process enriched the chemical composition of the nanocomposite. High-resolution C 1s spectra of 20%-BC/VE is presented in Figure 3 (d) while O 1s spectra of 20%-BC/VE and C 1s spectra of bm-BC are included in supporting information (Figure S3). The presence of C species in the synthesized composite is evidenced by the same intensity peak of C 1s spectrum at binding energy 285 eV in bm-BC and 20%-BC/VE, which can be attributed to C-H (Oswald et al., 2017). The obviously different intensity range at binding energy 294.51 eV and 292.89 eV in 20%-BC/VE can be respectively assigned to π-electron and π-π^* shake-up satellite band of graphitic carbons (Aguirre-Araque et al., 2019; Faheem et al., 2016). The separate peak at 283.71 eV in 20%-BC/VE can be assigned to chemical bonds Al-O-C (Liu et al., 2016).

3.3 Adsorption kinetics and isotherm

The adsorption kinetics of As(V) onto 20%-BC/VE is illustrated in Figure 4a. After rapid rate in the initial 12 h, As (V) adsorption slowed down and did not reach adsorption equilibrium until about 36 h. Three kinetics models were explored (S1, supporting information), and the pseudo-second order kinetics model matched the experimental data slightly better (R^2=0.99) than the pseudo-first order kinetics model (R^2=0.978), and the simple Elovich model (R^2=0.984) (Figure 4a). The equilibrium adsorption capacity (q_e) predicted by the pseudo- first and second order models were 6.5 mg $g^{-1}$and 7.5 mg g^{-1}, close to the experimental data (6.9 mg g^{-1}). The reported q_e of As(V) onto different adsorbents are summarized in Table 2.

The Elovich model is a useful tool in describing sorption on highly heterogeneous adsorbent surface (Pęgier et al., 2019). The predicted plot of the Elovich model suggested that the adsorption mechanisms of As(V) onto 20%-BC/VE were not only influenced by physisorption, but also controlled by the chemisorption (Vithanage et al., 2016). Thus, the adsorption rate can be controlled by both number of active sites on the surface of adsorbent and intra-particle diffusion process inferred from the two segments of simulation plot of the inter-particle diffusion model using kinetics adsorption data versus $t^{0.5}$ (Figure 4b) (Vasudevan et al., 2016).

The obtained experimental data fitted well to both Langmuir and Freundlich isotherm models (S2, Supporting information) with R^2 values ranging from 0.955 to close to 1 (Figure 4b). The predicted the maximum adsorption capacity (q_m) of As(V) onto 20%-BC/VE was 20.1 mg g^{-1}. The 20%-BC/VE has excellent adsorption efficiency for As(V) removal compared with different adsorbents reported in the literature (Table 2).

The enhanced As(V) adsorption ability of the ball-milled BC/VE nanocomposite can be attributed to following two perspectives. First, ball milling proper proportion of BC particles into the interlaminar structure of VE may increase its interlayer distance to expose the exchangeable anions and positively charged surface sites, which can promote the adsorption of As(V) through ion exchange and electrostatic attraction, respectively. Excessive BC, however, would fill the interlayer space of VE, hindering the adsorption of As(V). Second, ball milling may initiate cationic activation of Ca/Fe/Al/Mg minerals (M^{n+}) that exist in the crystal cells of VE to serve as the adsorption sites for As(V). The interactions between As(V) and the activated minerals can be expressed as (Wang et al., 2018):

$$S-M^{n+}+\frac{n}{i-3}H_iAsO_4^{\,i-3}\rightarrow S-M^{n+}\cdots(H_iAsO_4^{\,i-3})_{\frac{n}{i-3}} \quad (1)$$

$$S-M^{n+}\cdots(OH^-)_n+\frac{n}{i-3}H_iAsO_4^{\,i-3}\rightarrow S-M^{n+}\cdots(H_iAsO_4^{\,i-3})_{\frac{n}{i-3}}+n(OH^-) \quad (2)$$

where S denotes the surface of the nanocomposite and $i = 0$, 1, or 2.

3.4 The influence of pH, coexisting anions, and soluble organic matter

The initial pH of testing solution affects the speciation distribution of As(V) ions, namely $H_2AsO_4^-$, $HAsO_4^{2-}$, and AsO_4^{3-}. Figure 5a shows their relative percentage at varying solution pH calculated by the open source software Visual MINTEQ (31). For solution pH range of 2–6, the predominant As(V) species are $H_2AsO_4^-$ and H_3AsO_4 and the percentage of $H_2AsO_4^-$ increases as solution pH increases. For solution pH range of 6–8 the predominant As(V) species are $H_2AsO_4^-$ and $HAsO_4^{2-}$, and the percentage of $HAsO_4^{2-}$ increases as solution pH increases. Because the surface of BC/VE nanocomposites is variably charged depending on solution pH, the electrostatic attraction between As(V) species and the 20%-BC/VE adsorbent also changes with solution pH. Figure 5b shows that As(V) adsorption increased from 5.62 mg g^{-1} to 7.12 mg g^{-1} as pH value increased from 4.0 to 6.0, likely corresponding to the increase in $H_2AsO_4^-$ and decrease in H_3AsO_4. In contrast, further increase in the initial pH reduced As (V) adsorption. At pH 8.0, As(V) adsorption capacity was only 5.43 mg g^{-1}. The optimal initial pH of 6.0 for As(V) removal is consistent with previous studies (Chammui et al., 2014; He et al., 2018; Jeon et al., 2018).

The 20%-BC/VE adsorbent was examined in the presence of humic acid (1, 3, 5, 8, and 10 mg L^{-1}). The results indicated that humic acid has no obvious inhibitory effect on As(V) adsorption (Figure 5c). In other words, the tested adsorbent possesses good selective adsorption performance for As(V). It might be due to the size exclusion effect that HA macromolecules were too large to diffuse into the interlayers/pores of the nanocomposite.

The coexisting anions were documented to decrease the As(V) adsorption due to the competition for electrostatic attraction (Li et al., 2016a; Navarathna et al., 2019). However, our results indicated that the effects of coexisting SO_4^{2-}, NO_3^-, Cl^- of the same moles with As(V) were insignificant (Figure 5d). Previous studies have also noted that the effects of coexisting anions on As(V) removal, though decreasing following the order of $SO_4^{2-} > NO_3^- > Cl^-$, are minimal until exceeding a critical concentration e.g., SO_4^{2-} concentration at 50 times of As(V) (Chammui et al., 2014). However, the presence of PO_4^{3-} at the same concentration with As(V) reduced As(V) adsorption by about 50%. The strong effect of phosphate on As(V) adsorption is because both arsenate and phosphate are tetrahedral oxyanions and they compete for adsorption sites in solution (Manning and Goldberg, 1996).

4. Conclusions

We can conclude that the 20%-BC/VE nanocomposite can serve as a superior adsorbent for As(V) adsorption, with 20.1 mg/g As(V) Langmuir isotherm capacity. This ball milled nanocomposite possessed much higher SSA and PV (2–6 times) than their pristine counterparts. The incorporation of biochar into the hybrid particles caused notable changes to the crystallinity of VE and activated the cations for enhanced adsorption performance for As(V). The 20%-BC/VE best performed at pH 6, and As(V) was not influenced by the presence of humic acid and anion competition (NO_3^-, Cl^-, SO_4^{2-}) except for PO_4^{3-}.

Supplementary Material

Refer to Web version on PubMed Central for supplementary material.

Acknowledgments

Fang Li would like to acknowledge the support of the National Natural Science Foundation of China (Grant No. 41807124) and the China Scholarship Council (File No. 201809135012). The views expressed in this article are those of the authors and do not necessarily reflect the views or policies of the U.S. Environmental Protection Agency.

References

Saleh AT, Sarı A, Tuzen M, 2016. Chitosan-modified vermiculite for As(III) adsorption from aqueous solution: Equilibrium, thermodynamic and kinetic studies. Journal of Molecular Liquids 219, 937–945.

Aglietti EF, Lopez JP, 1992. Physicochemical and thermal properties of mechanochemically activated talc. Materials Research Bulletin 27, 1205–1216.

Aguirre-Araque JS, Gonçalves JM, Nakamura M, Rossini PO, Angnes L, Araki K, Toma HE, 2019. GO composite encompassing a tetraruthenated cobalt porphyrin-Ni coordination polymer and its behavior as isoniazid BIA sensor. Electrochimica Acta 300, 113–122.

Alzaydien AS, 2016. Physical, Chemical and Adsorptive Characteristics of Local Oak Sawdust Based Activated Carbons. Asian Journal of Scientific Research 9, 45–56.

Aredes S, Klein B, Pawlik M, 2013. The removal of arsenic from water using natural iron oxide minerals. Journal of Cleaner Production 60, 71–76.

Bakshi S, Banik C, Rathke SJ, Laird DA, 2018. Arsenic sorption on zero-valent iron-biochar complexes. Water Res 137, 153–163. [PubMed: 29554531]

Basaleh AA, Al-Malack MH, Saleh TA, 2019. Methylene Blue removal using polyamide-vermiculite nanocomposites: Kinetics, equilibrium and thermodynamic study. Journal of Environmental Chemical Engineering 7, 103107.

Ben Ticha M, Haddar W, Meksi N, Guesmi A, Mhenni MF, 2016. Improving dyeability of modified cotton fabrics by the natural aqueous extract from red cabbage using ultrasonic energy. Carbohydr Polym 154, 287–295. [PubMed: 27577920]

Benbrahim-Tallaa L, Waalkes MP, 2008. Inorganic Arsenic and Human Prostate Cancer. Environmental Health Perspectives 116, 158–164. [PubMed: 18288312]

Chammui Y, Sooksamiti P, Naksata W, Thiansem S, Arqueropanyo O. a., 2014. Removal of arsenic from aqueous solution by adsorption on Leonardite. Chemical Engineering Journal 240, 202–210.

Chowdhury SR, Yanful EK, Pratt AR, 2010. Arsenic removal from aqueous solutions by mixed magnetite–maghemite nanoparticles. Environmental Earth Sciences 64, 411–423.

Faheem Yu H., Liu J, Shen J, Sun X, Li J, Wang L, 2016. Preparation of MnO x -loaded biochar for Pb 2+ removal: Adsorption performance and possible mechanism. Journal of the Taiwan Institute of Chemical Engineers 66, 313–320.

Gencel O, del Coz Diaz JJ, Sutcu M, Koksal F, Alvarez Rabanal FP, Martinez-Barrera G, Brostow W, 2014. Properties of gypsum composites containing vermiculite and polypropylene fibers: Numerical and experimental results. Energy and Buildings 70, 135–144.

Gude J, Rietveld L, Van Halem D, 2018. Biological As (III) oxidation in rapid sand filters. Journal of Water Process Engineering 21, 107–115.

He R, Peng Z, Lyu H, Huang H, Nan Q, Tang J, 2018. Synthesis and characterization of an iron-impregnated biochar for aqueous arsenic removal. Sci Total Environ 612, 1177–1186. [PubMed: 28892862]

Hu X, Ding Z, Zimmerman AR, Wang S, Gao B, 2015. Batch and column sorption of arsenic onto iron-impregnated biochar synthesized through hydrolysis. Water Res 68, 206–216. [PubMed: 25462729]

Huang J-H, Matzner E, 2006. Dynamics of organic and inorganic arsenic in the solution phase of an acidic fen in Germany. Geochimica et Cosmochimica Acta 70, 2023–2033.

Jeon E-K, Ryu S, Park S-W, Wang L, Tsang DCW, Baek K, 2018. Enhanced adsorption of arsenic onto alum sludge modified by calcination. Journal of Cleaner Production 176, 54–62.

Jin L, Dai B, 2012. Preparation and Properties of Zno/Vermiculite Composite Particles. Advanced Materials Research 455-456, 265–270.

Li H, Shan C, Zhang Y, Cai J, Zhang W, Pan B, 2016a. Arsenate Adsorption by Hydrous Ferric Oxide Nanoparticles Embedded in Cross-linked Anion Exchanger: Effect of the Host Pore Structure. ACS Appl Mater Interfaces 8, 3012–3020. [PubMed: 26765396]

Li J, Hitch M, 2016. Characterization of the microstructure of mechanically-activated olivine using X-ray diffraction pattern analysis. Minerals Engineering 86, 24–33.

Li W, Chen D, Xia F, Tan JZ, Huang P-P, Song W-G, Nursam NM, Caruso RA, 2016b. Extremely high arsenic removal capacity for mesoporous aluminium magnesium oxide composites. Environmental Science: Nano 3, 94–106.

Liu H, Chen G, Jiang H, Guo D, Yan Z, Wu X, Li P, Wang X, 2016. Performance and mechanism of laser transmission joining between glass fiber-reinforced PA66 and PC. Journal of Applied Polymer Science 133, n/a-n/a.

Liu TY, Ma Y, Yu SF, Shi J, Xue S, 2011a. The effect of ball milling treatment on structure and porosity of maize starch granule. Innovative Food Science & Emerging Technologies 12, 586–593.

Liu Y, Li Q, Gao S, Shang JK, 2011b. Exceptional As (III) sorption capacity by highly porous magnesium oxide nanoflakes made from hydrothermal synthesis. Journal of the American Ceramic Society 94, 217–223.

Lu H, Liu X, Liu F, Hao Z, Zhang J, Lin Z, Barnett Y, Pan G, 2019. Visible-light photocatalysis accelerates As(III) release and oxidation from arsenic-containing sludge. Applied Catalysis B: Environmental 250, 1–9.

Lyu H, Gao B, He F, Zimmerman AR, Ding C, Huang H, Tang J, 2018. Effects of ball milling on the physicochemical and sorptive properties of biochar: Experimental observations and governing mechanisms. Environ Pollut 233, 54–63. [PubMed: 29053998]

Malandrino M, Abollino O, Buoso S, Giacomino A, La Gioia C, Mentasti E, 2011. Accumulation of heavy metals from contaminated soil to plants and evaluation of soil remediation by vermiculite. Chemosphere 82, 169–178. [PubMed: 21055788]

Manning BA, Goldberg S, 1996. Modeling arsenate competitive adsorption on kaolinite, montmorillonite and illite. Clays and clay minerals 44, 609–623.

Miner CS, 1934. Production of expanded vermiculite. Google Patents.

National Research C, 1977. Medical and Biological Effects of Environmental Pollutants, Arsenic: Medical and Biologic Effects of Environmental Pollutants. The National Academies Press (US), Washington, DC.

National Research C, 1999. Arsenic in Drinking Water. The National Academies Press, Washington, DC.

National Research C, 2001. Arsenic in Drinking Water: 2001 Update. The National Academies Press, Washington, DC.

Navarathna CM, Karunanayake AG, Gunatilake SR, Pittman CU Jr., Perez F, Mohan D, Mlsna T, 2019. Removal of Arsenic(III) from water using magnetite precipitated onto Douglas fir biochar. J Environ Manage 250, 109429. [PubMed: 31491719]

Oswald S, Hoffmann M, Zier M, 2017. Peak position differences observed during XPS sputter depth profiling of the SEI on lithiated and delithiated carbon-based anode material for Li-ion batteries. Applied Surface Science 401, 408–413.

Park H, Myung NV, Jung H, Choi H, 2008. As(V) remediation using electrochemically synthesized maghemite nanoparticles. Journal of Nanoparticle Research 11, 1981–1989.

Pęgier M, Kilian K, Pyrzynska K, 2019. Kinetics of scandium ion sorption onto oxidized carbon nanotubes. Monatshefte für Chemie - Chemical Monthly 150, 1569–1572.

Sattar MS, Shakoor MB, Ali S, Rizwan M, Niazi NK, Jilani A, 2019. Comparative efficiency of peanut shell and peanut shell biochar for removal of arsenic from water. Environ Sci Pollut Res Int 26, 18624–18635. [PubMed: 31055751]

Shen T, Ge W, Wang K, Quan M, Wang J, Wei W, Koch C, 1996. Structural disorder and phase transformation in graphite produced by ball milling. Nanostructured materials 7, 393–399.

Shumlas SL, Singireddy S, Thenuwara AC, Attanayake NH, Reeder RJ, Strongin DR, 2016. Oxidation of arsenite to arsenate on birnessite in the presence of light. Geochemical transactions 17, 5. [PubMed: 28316506]

Silva A, Martinho S, Stawinski W, Wegrzyn A, Figueiredo S, Santos L, Freitas O, 2018. Application of vermiculite-derived sustainable adsorbents for removal of venlafaxine. Environ Sci Pollut Res Int 25, 17066–17076. [PubMed: 29637454]

Singh R, Singh S, Parihar P, Singh VP, Prasad SM, 2015. Arsenic contamination, consequences and remediation techniques: a review. Ecotoxicol Environ Saf 112, 247–270. [PubMed: 25463877]

Sugawara K, Kanamori S, 1964. The spectrophotometric determination of trace amounts of arsenate and arsenite in natural waters with special reference to phosphate determination. Bulletin of the Chemical Society of Japan 37, 1358–1363.

Suriyagoda LDB, Dittert K, Lambers H, 2018. Arsenic in Rice Soils and Potential Agronomic Mitigation Strategies to Reduce Arsenic Bioavailability: A Review. Pedosphere 28, 363–382.

Tuchowska M, Wołowiec M, Solińska A, Kościelniak A, Bajda T, 2019. Organo-Modified Vermiculite: Preparation, Characterization, and Sorption of Arsenic Compounds. Minerals 9, 483.

Vasudevan M, Ajithkumar PS, Singh RP, Natarajan N, 2016. Mass transfer kinetics using two-site interface model for removal of Cr(VI) from aqueous solution with cassava peel and rubber tree bark as adsorbents. Environmental Engineering Research 21, 152–163.

Vithanage M, Mayakaduwa SS, Herath I, Ok YS, Mohan D, 2016. Kinetics, thermodynamics and mechanistic studies of carbofuran removal using biochars from tea waste and rice husks. Chemosphere 150, 781–789. [PubMed: 26607239]

Wang J, Zhang T, Li M, Yang Y, Lu P, Ning P, Wang Q, 2018. Arsenic removal from water/wastewater using layered double hydroxide derived adsorbents, a critical review. RSC Advances 8, 22694–22709. [PubMed: 35539721]

Yao Y, Jin J, Liu D, Wang Y, Kou X, Lin Y, 2016. Evaluation of Vermiculite in Reducing Ash Deposition during the Combustion of High-Calcium and High-Sodium Zhundong Coal in a Drop-Tube Furnace. Energy & Fuels 30, 3488–3494.

Zhang M, Gao B, Varnoosfaderani S, Hebard A, Yao Y, Inyang M, 2013a. Preparation and characterization of a novel magnetic biochar for arsenic removal. Bioresour Technol 130, 457–462. [PubMed: 23313693]

Zhang M, Gao B, Yao Y, Inyang M, 2013b. Phosphate removal ability of biochar/MgAl-LDH ultra-fine composites prepared by liquid-phase deposition. Chemosphere 92, 1042–1047. [PubMed: 23545188]

Zhang W, Singh P, Paling E, Delides S, 2004. Arsenic removal from contaminated water by natural iron ores. Minerals Engineering 17, 517–524.

Zheng Y, Wang B, Wester AE, Chen J, He F, Chen H, Gao B, 2019a. Reclaiming phosphorus from secondary treated municipal wastewater with engineered biochar. Chemical Engineering Journal 362, 460–468.

Zheng Y, Yang Y, Zhang Y, Zou W, Luo Y, Dong L, Gao B, 2019b. Facile one-step synthesis of graphitic carbon nitride-modified biochar for the removal of reactive red 120 through adsorption and photocatalytic degradation. Biochar 1, 89–96.

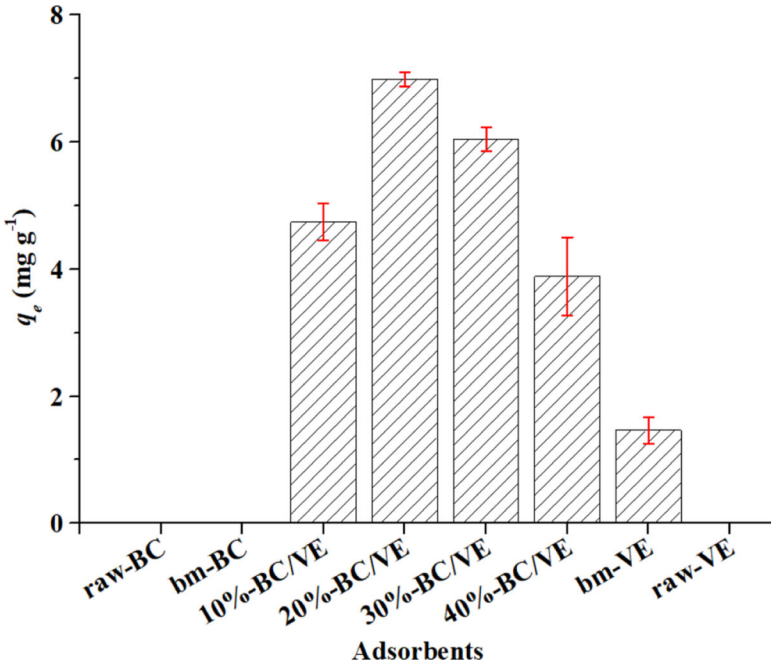

Figure 1.
As(V) sorption capacity onto BC/VE composites in different weight ratios and raw materials.

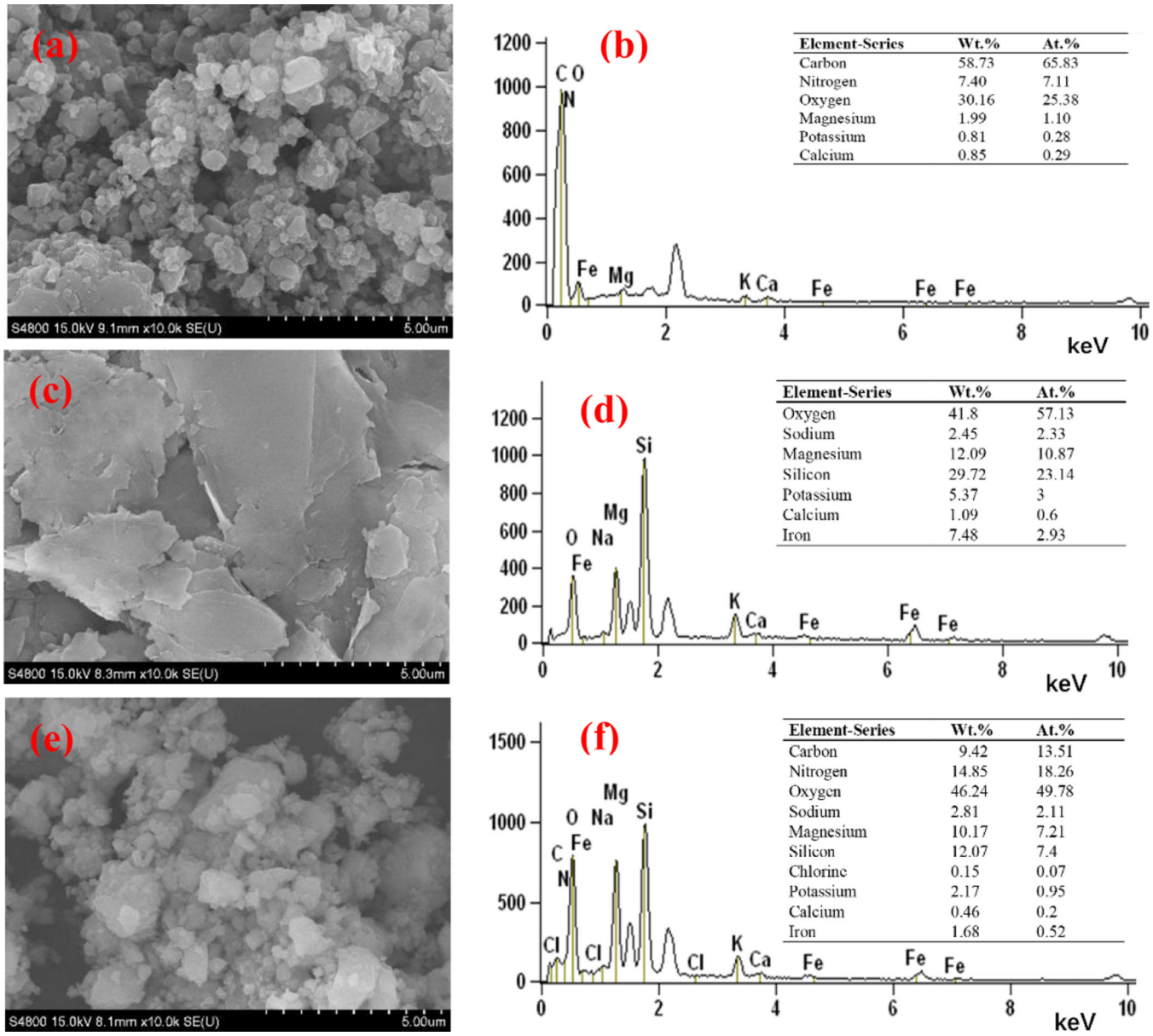

Figure 2.

SEM images of (a) bm-BC, (c) bm-VE, and (e) 20%-BC/VE, and EDS spectra of (b) bm-BC, (d) bm-VE, and (f) 20%-BC/VE samples.

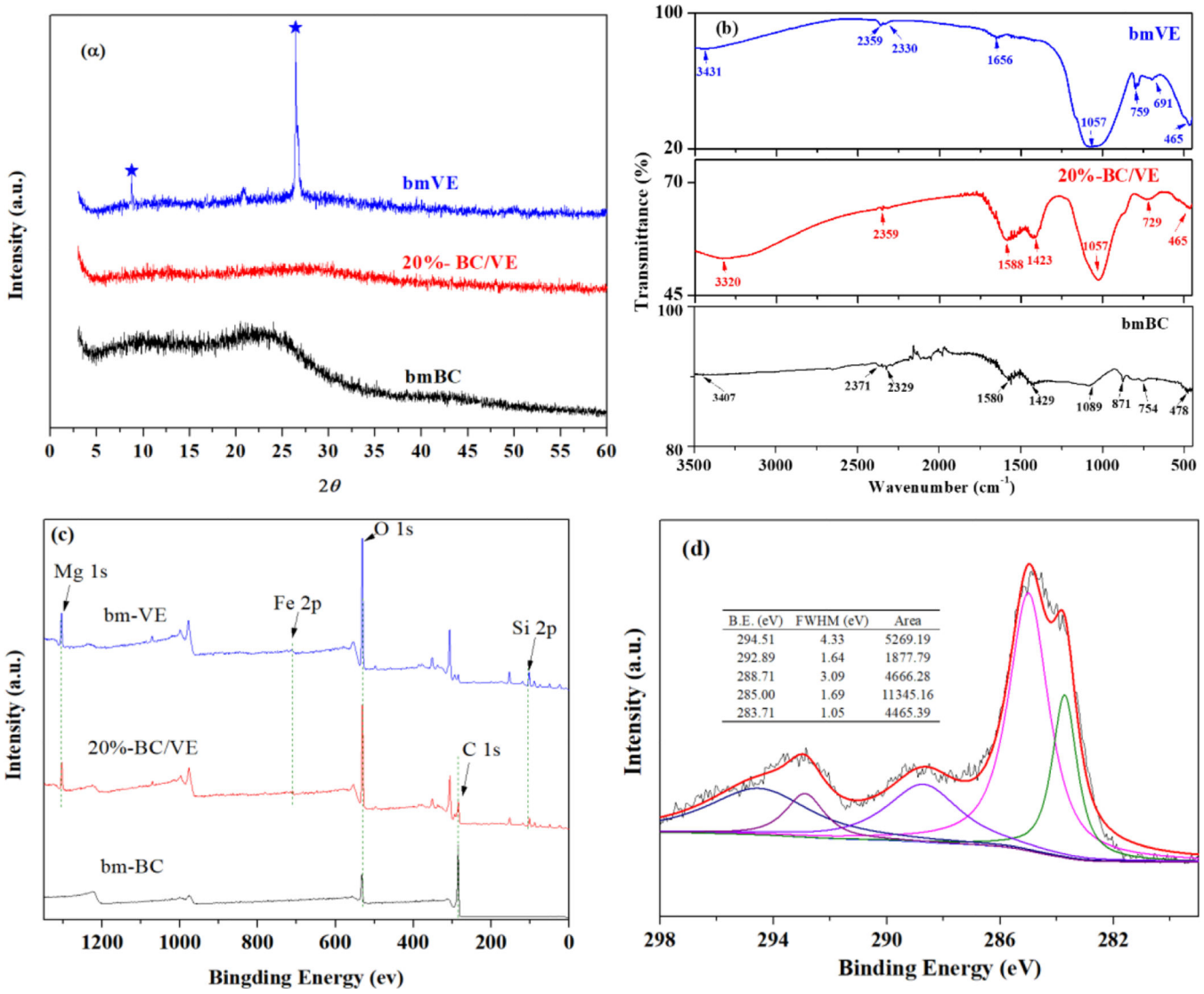

Figure 3.

(a) XRD patterns, (b) FT-IR spectra, (c) XPS survey sacn of bm-BC, bm-VE, and 20%-BC/VE, (d) C1s XPS spectra of 20%-BC/VE.

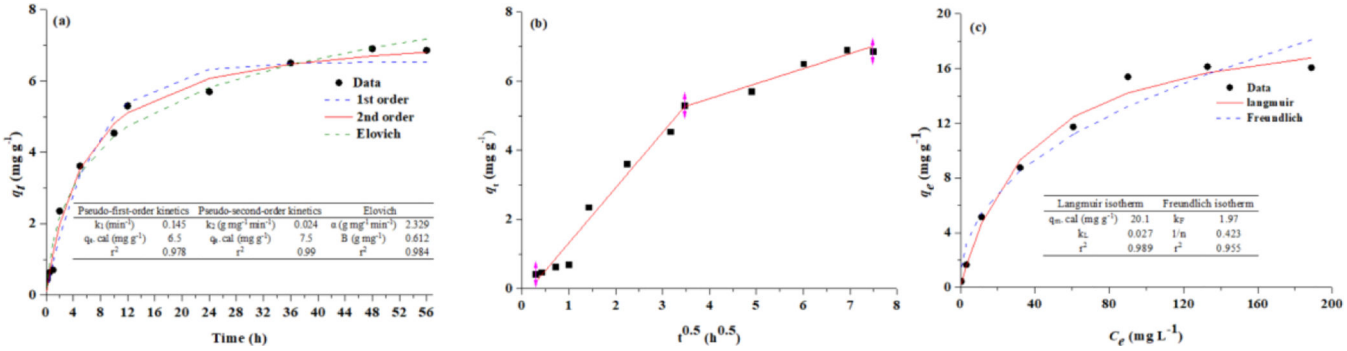

Figure 4.

(a) Adsorption kinetics of As(V) adsorption onto 20%-BC/VE, (b) kinetics of As(V) adsorption (vs. squre root of time), and (c) isotherms of As(V) adsorption onto 20%-BC/VE. The red lines are simulations of various models.

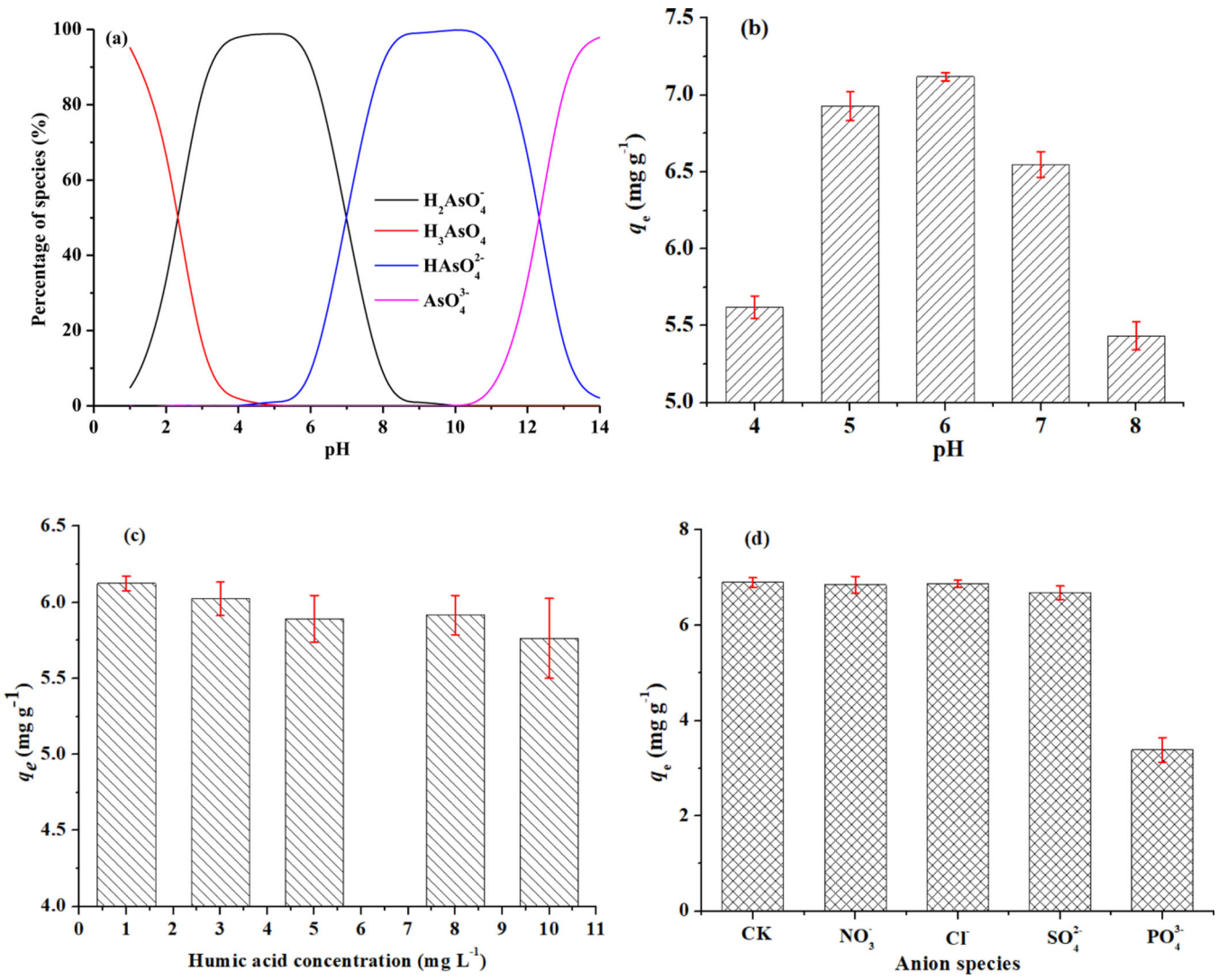

Figure 5.

(a) As(V) speciation simulated using Visual MINTEQ(Version 3.1). Effects of (b) initial solution pH, (c) humic acid concentration, and (d) coexisting anion on the adsorption of As(V) by 20%-BC/VE.

Table 1.

Properties of the adsorbents.

Samples	Surface Area (m^2 g^{-1})	Pore Volume (cm^3 g^{-1})	Pore Size (nm)
raw-BC	214.6219	0.0094	1.1403
bm-BC	286.4478	0.0995	0.5874
raw-VE	4.8858	0.0272	29.8226
bm-VE	2.8660	0.0188	35.5583
20%-BC/VE	16.0779	0.0466	12.9292

Table 2.

Reported As(V) adsorption capacities of various adsorbents.

Adsorpent	Kinetics model	q_e (mg g $^{-1}$)	Isotherm model	q_m mg g $^{-1}$)	Initial concentration (mg l^{-1})	pH	Reference
Maghemite nano particles	2h, Pseudo 1st and 2nd order	NA	Langmuir and Freundlich	4.64	1	7	(Park et al., 2008)
Magnetite-maghemite	3h, two steps	4.85	Langmuir	6	2	6.5	(Chowdhury et al., 2010)
Biochar/γ -Fe_2O_3	24h, Pseudo 2nd order	3.525	Langmuir	3.147	50	NA	(Zhang et al., 2013a)
ZVI-RO ZVISG	48h, Pseudo 2nd order	15.87 6.94	Langmuir	15.58 7.92	25	NA	(Bakshi et al., 2018)
Peanut shell biochar	Pseudo 1st and 2nd order	4.76	Langmuir, Freundlich, and others	7.94	5	5.4	(Sattar et al., 2019)
20%-BC/VE	48h, Pseudo 2nd order	6.5	Langmuir	20.1	20		This study